An Electron Density Model of the D- and E-region Ionosphere for Transionospheric VLF Propagation

Wei Xu[1], Robert A. Marshall[1], Jacob Bortnik[2], and John W. Bonnell[3]

[1]Department of Aerospace Engineering Sciences, University of Colorado Boulder, Boulder, CO, USA.
[2]Department of Atmospheric and Oceanic Sciences, University of California Los Angeles, Los Angeles, CA, USA.
[3]Space Sciences Laboratory, University of California Berkeley, Berkeley, CA, USA.

Key Points:

- We describe an electron density model of the D- and E-region ionosphere for transionospheric VLF propagation
- We parameterize the Faraday International Reference Ionosphere model and extend the Wait and Spies profile to E-region altitudes
- We calculate the expected transmitter signal under the full range of possible ionosphere conditions for lower ionosphere remote sensing

Corresponding author: Wei Xu, `Wei-Xu@colorado.edu`

Abstract

Terrestrial Very-Low-Frequency (VLF) energy from both lightning discharge and radio transmitters has a role in affecting the energetic electrons in the Van Allen radiation belts, but quantification of these effects is particularly difficult, largely due to the collisional damping experienced in the highly-variant electron density in the D- and E-region ionosphere. The Faraday International Reference Ionosphere (FIRI) model was specifically developed by combining lower-ionosphere chemistry modeling with in situ rocket measurements, and represents to date the most reliable source of electron density profiles for the lower ionosphere. As a full-resolution empirical model, FIRI is not well suited to D- and E-region ionosphere inversion, and its applicability in transionospheric VLF simulation and in remote sensing of the lower ionosphere is limited. Motivated by how subionospheric VLF remote sensing has been aided by the Wait and Spies (WS) profile [*Wait and Spies*, 1964], in this study, we parameterize the FIRI profiles and extend the WS profile to the E-region ionosphere by introducing two new parameters: the knee altitude h_{k} and the sharpness parameter for the E-region ionosphere β_{E}. Using this modified WS profile, we calculate the expected signals at different receiver locations from the NAA, NPM, and NWC transmitters under the full range of possible ionospheric conditions. We also describe and validate a method about how these results can be readily used to translate VLF measurements into estimates of the lower ionosphere electron density. Moreover, we use this method to evaluate the sensitivity of different ground receiver locations in lower-ionosphere remote sensing.

1 Introduction

Because of solar radiation, the Earth's atmosphere at thermospheric altitudes becomes weakly ionized and forms a natural 'plasma' roof known as the ionosphere [e.g., *Budden*, 1998]. The extent of ionization in the ionosphere exhibits great variation depending on the altitude, time of the day, season, latitude, longitude, the abundance of neutral species, and solar activity [e.g., *Jursa*, 1985]. Based on the local maxima in the vertical profile of electron density, the Earth's ionosphere is customarily divided into a number of characteristic regions [e.g., *Budden*, 1998]: the D-region (60–90 km), the E-region (90–150 km), and the F-region (150–500 km). The electron concentration in the F-region constitutes most of the total electron content (TEC) and is due primarily to ionization of atomic oxygen and molecular nitrogen by solar extreme-ultraviolet radiation [*Brasseur and Solomon*, 2006]. As for the D- and E-regions, the main source of free electrons is photoionization of NO by Lyman-α radiation, and ionization of molecular and atomic oxygen, and molecular nitrogen by solar X-rays and Lyman-β radiation, respectively [*Brasseur and Solomon*, 2006].

As the transition area between the neutral atmosphere and the central ionosphere, the D- and E-regions play a pivotal role in aeronomy and space physics research. Phenomena that are affected by these regions include atmospheric gravity waves [e.g., *Fritts and Alexander*, 2003], radiation belt particle precipitation [e.g., *Codrescu et al.*, 1997], and solar perturbations such as flares [e.g., *Han and Cummer*, 2010] and eclipses [e.g., *Xu et al.*, 2019]. In particular, the dynamics of these two regions is critical for the propagation, reflection, and dissipation of Very-Low-Frequency (VLF) waves (3–30 kiloHertz, kHz) [*Lehtinen and Inan*, 2009]. Terrestrial VLF waves, both natural from lightning flashes and artificial from ground-based transmitters, are reflected by the sharp boundary of electron density in the D-region ionosphere and are thus trapped within the Earth-Ionosphere (EI) waveguide, especially during daytime conditions [*Budden*, 1998]. As such, VLF remote sensing techniques have been commonly used for thunderstorm study and tracking [e.g., *Inan et al.*, 2010], long-range communication [e.g., *Hosseini et al.*, 2019], as well as remote sensing of the ionosphere state [e.g., *Han et al.*, 2011; *Marshall and Snively*, 2014]. At nighttime, a large fraction of the bottom side ionospheric plasma recombines, and a small but geophysically significant portion of terrestrial VLF energy leaks into the magnetosphere, and can potentially interact with the energetic electrons that constitute the radiation belts [*Vampola and Kuck*, 1978; *Imhof et al.*, 1983; *Platino et al.*, 2006; *Parrot et al.*, 2007; *Graf et al.*, 2011].

Through decades of observational and theoretical studies, it has been revealed that terrestrial VLF energy has a significant effect on energetic electron populations in the inner radiation belts [e.g., *Abel and Thorne*, 1998a,b; *Clilverd et al.*, 2008], as well as maintaining the slot region between the inner and outer radiation belts [*Abel and Thorne*, 1998a,b]. Lightning return strokes are the most powerful radiators of VLF waves on the Earth, and the leakage of lightning-generated VLF energy out of the EI waveguide can ultimately lead to scattering and precipitation of trapped radiation belt electrons [e.g., *Voss et al.*, 1984; *Bortnik et al.*, 2006a,b]. As for ground transmitters, observations from both the Detection of Electro-Magnetic Emissions Transmitted from Earthquake Regions (DEMETER) satellite and Van Allen Probes have shown that artificial VLF transmitters sometimes serve as the dominant source for the loss of relativistic radiation belt electrons at low L-shells [e.g., *Graf et al.*, 2009; *Foster et al.*, 2016; *Ma et al.*, 2017; *Claudepierre et al.*, 2020a,b]. More recent studies [*Hua et al.*, 2020] have also found direct evidence that VLF emissions from ground transmitters are capable of bifurcating radiation belt electrons at energies of tens of kiloelectronvolts (keV). Nevertheless, quantification of these effects on the radiation belts from a modeling perspective is made difficult by the complexity of transionospheric propagation of VLF waves, largely due to the highly-variant D- and E-region densities.

In general, absorption of terrestrial VLF waves occurs predominantly within the D- and lower E-region ionosphere (~60–110 km) [*Lehtinen and Inan*, 2009], and is controlled jointly by the electron and neutral densities in this altitude range [e.g., *Tao et al.*, 2010], with a minor influence from the Earth's magnetic field [*Graf et al.*, 2013]. In the majority of previous studies on this topic, attenuation of VLF waves through the ionosphere was taken into account using Helliwell's curves, which describe VLF absorption at 2 and 20 kHz and at different geomagnetic latitudes [*Helliwell*, 1965]. However, it has been later pointed out that Helliwell's curves underestimate VLF attenuation at 20 kHz by up to ~10 dB during daytime conditions, and up to ~20 dB during nighttime conditions [*Starks et al.*, 2008]. Many studies have since been devoted to resolving this discrepancy [e.g., *Tao et al.*, 2010; *Cohen et al.*, 2012; *Graf et al.*, 2013] and the works of *Tao et al.* [2010]; *Graf et al.* [2013] are particularly noteworthy. The authors have recalculated the absorption curve of VLF waves using more realistic ionosphere profiles, and investigated the dependence on ionospheric electron density [*Tao et al.*, 2010], as well as wave polarization, incidence angle, bearing, and ground conductivity [*Graf et al.*, 2013]. The uncertainty in VLF absorption among previous studies has been suggested to arise in large part from the case-to-case variation in ionospheric electron densities; the importance of the ionosphere variation has been repeatedly emphasized in the conclusion of both studies [*Tao et al.*, 2010; *Graf et al.*, 2013].

The electron density in the lower E- and D-regions of the ionosphere is not only highly variant, but extremely difficult to measure, since this altitude range is too low for spaceborne instruments and too high for balloon-borne instruments. High-power incoherent scatter radars (ISRs) require long integration time and enhanced ionization rate, and are available at limited locations [*Friedrich et al.*, 2018]. Riometers infer the ionosphere electron density by measuring the radio wave absorption along the propagation path [*McKay-Bukowski et al.*, 2015], predominantly in the D-region. Ionosondes are more sensitive to the electron density above the E-region, while GPS measurements provide an integrated line of sight measurement and are dominantly controlled by the F-region density [*Bilitza*, 2001]. The VLF technique is effective at remotely sensing the D-region ionosphere, but, in most cases, only estimates the reflection altitude of VLF waves and the steepness of the electron density profile below this altitude. Overall, in situ rocket measurements are so far the most accurate approach. From the 1960s to 1970s, several hundreds of sounding rockets were launched to record the ionosphere neutral and plasma densities at different latitudes and solar zenith angles; these rocket data have been later used as the basis for the development of a D- and E-region electron density model [*Friedrich and Torkar*, 2001].

Various empirical and first-principles electron density models have been proposed for the ionosphere, with the most widely used undoubtedly being the International Reference Ionosphere (IRI) [*Bilitza*, 2001]. As the international standard for the specification of ionosphere conditions, IRI has been routinely used in a wide variety of studies ranging from heliophysics to atmospheric research. However, as pointed out by *Friedrich et al.* [2018], most of the electron density data upon which IRI was built are insensitive to the D- and lower E-region, and the accuracy of IRI in this altitude range is insufficient. On the other hand, a semiempirical model has been specifically proposed to address the inaccuracies in these two regions: the Faraday International Reference Ionosphere (FIRI) [*Friedrich and Torkar*, 2001]. FIRI is explicitly developed by combining lower-ionosphere chemistry modeling and rocket-measured electron density profiles [*Friedrich et al.*, 2001], and represents to date the most reliable source of electron density for D- and E-region ionosphere. Note that earlier versions of the IRI model provided FIRI data as an option for the electron density in the lower ionosphere. Because of model compatibility issues, starting from the 2007 version of IRI, FIRI has been provided as a standalone model [*Bilitza and Reinisch*, 2008]. Despite being reliable, FIRI profiles, as a collection of electron density profiles at different geolocations under different solar zenith angles, were mostly utilized to estimate the statistical bounds on VLF absorption curves [*Tao et al.*, 2010; *Graf et al.*, 2013]. As a full-resolution empirical model, FIRI as-is is not well suited to D- and E-region ionosphere inversion; the applicability of FIRI in transionospheric VLF simulations, as well as lower ionosphere remote sensing, is limited.

The VLF technique has been highly successful at remote sensing the subionospheric state, largely with the aid of a parameterized electron density model for the D-region ionosphere: the well-known Wait and Spies (WS) profile [*Wait and Spies*, 1964]. This profile approximates the electron density below the reflection altitudes of VLF waves using an exponential function with two parameters: a characteristic height (h') and a sharpness parameter (β). The D-region electron density is then derived by finding the pair of h' and β values that best explains VLF measurements. Motivated by how subionospheric VLF remote sensing has been aided by the WS profile, in this study, we parameterize the FIRI profiles and extend the WS profile to E-region altitudes by introducing two additional parameters. *Cummer and Inan* [2000] have also extended the WS profile to E-region altitudes, but using different parameters and for the purpose of E-region remote sensing using lightning-emitted Extreme-Low-Frequency (ELF) waves. Developing such a parameterized semi-analytical electron density model thus enables us to perform parametric studies and tabulate the one-to-one relation between VLF absorption and different ionosphere conditions. Using this modified WS profile, we calculate the expected signals at different receiver locations from the NAA, NPM, and NWC transmitters under all ionosphere conditions, i.e., a lookup table. We also explain and demonstrate how this lookup table can be directly used to translate VLF measurements into estimates of ionosphere electron density.

2 D- and E-region Electron Density

2.1 The Faraday International Reference Ionosphere

FIRI was first released in 2001 for describing the electron density in the D- and E-regions of the ionosphere (55–150 km) during nonauroral conditions [*Friedrich and Torkar*, 2001]. This model was developed by adjusting results of lower-ionosphere chemistry modeling using data collected from Faraday rotation experiments on sounding rockets [*Friedrich et al.*, 2001]. Over the past few decades, FIRI has been updated by excluding questionable rocket data and including Langmuir probe data for the altitude range from 51 to 90 km [*Friedrich et al.*, 2018]. The 2018 version of FIRI contains a total of 1,980 profiles of electron densities between 55 and 150 km altitude, covering 11 solar zenith angles from 0 to 130°, and latitudes at 0°, 15°, 30°, 45° and 60°, with 1,620 profiles for the daytime ionosphere and another 360 profiles for the nighttime ionosphere [*Friedrich et al.*, 2018].

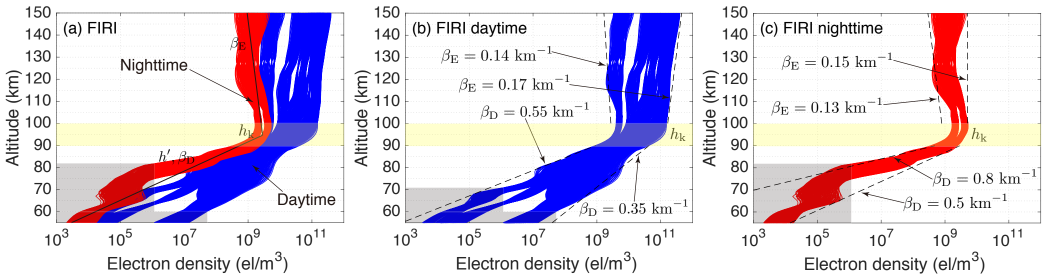

Figure 1. (a) FIRI profiles of electron density in the D- and E-regions of the ionosphere (55–150 km) for both daytime (blue) and nighttime (red) conditions. FIRI profiles can be approximated using four parameters: characteristic height h' [km], sharpness parameter for the D-region ionosphere β_D [km^{-1}], knee altitude h_k [km], and sharpness parameter for the E-region ionosphere β_E [km^{-1}]. The yellow shaded area marks the altitude range in which the slope of electron density profile changes. The gray shaded area marks the altitude and electron density range in which the FIRI profiles are considered to be less accurate [*Friedrich et al.*, 2018]. Typical values of β_D, h_k, and β_E for (b) daytime and (c) nighttime FIRI profiles. A total of 1,620 and 360 profiles are shown for the daytime and nighttime conditions, respectively.

Figure 1 shows FIRI profiles of the electron density in the D- and E-region ionosphere. The blue curves show daytime electron density profiles, while red curves show those of nighttime. The yellow shaded area marks the altitude range in which the slope of electron density profile changes. The gray shaded area marks the altitude and electron density range in which the FIRI profiles are considered to be less accurate [*Friedrich et al.*, 2018]. Below ~90 km, the majority of the daytime FIRI profiles can be satisfactorily fitted using a single exponential function (Figure 1b), i.e., the WS profile. Moreover, for both daytime and nighttime FIRI profiles, the slope of the electron density in the D-region is notably different from that in the E-region, and the WS formula becomes no longer valid for the E-region.

It is important to note that, as explained in *Friedrich et al.* [2018], the FIRI profiles are valid at the altitudes above 60 km and densities larger than 10^6 m^{-3}. The sudden jump in the electron density profile around ~70 km (see Figure 1c) could be unphysical. We emphasize that, even though the FIRI model is considered to be less accurate at altitudes below 60 km and electron density less than 10^6 m^{-3}, it is not critical in the present study since this inaccurate region is only related to the parameters h' and β in the WS profile [*Wait and Spies*, 1964], which have been extensively used and validated in previous studies.

2.2 The Modified Wait and Spies Profile

To capture the two-segment feature of FIRI profiles, we extend the WS profile and introduce two parameters for the E-region: a knee altitude h_k [km] – the altitude starting from which the slope of electron density becomes notably different from that in D-region – and a sharpness parameter for the E-region ionosphere β_E [km^{-1}]. These two parameters are motivated by the "knee"-like structure of the FIRI profiles, which has also been used for describing the atmospheric conductivity [e.g., *Mushtak and Williams*, 2002; *Yang and Pasko*, 2005]. With h_k and β_E, the electron density at altitude h [km] below 150 km can be calculated in a unified fashion:

$$n_e(h) = \begin{cases} 1.43 \times 10^{13} e^{-0.15h'} e^{(\beta_D - 0.15)(h-h')}, \text{for } h \le h_k \\ n_e(h_k) e^{(\beta_E - 0.15)(h-h_k)}, \text{for } h_k < h \le 150 \text{ km} \end{cases} \tag{1}$$

In this model, the electron density below h_k is exactly the WS profile; h' [km] is the characteristic height and β_D [km^{-1}] is the sharpness parameter of the D-region ionosphere (same as β in the WS profile). Typical values are h' = 65–75 km for daytime, and 75–90 km for nighttime [*Marshall et al.*, 2017]. The typical range of β_D is 0.3–0.5 km^{-1} for daytime, and 0.5–0.8 km^{-1} for nighttime [*Marshall et al.*, 2017]. For both daytime and nighttime, the altitude above which the slope of the electron density profiles becomes different from that in the D-region is around 90–100 km (marked as shaded area in Figure 1), and thus h_k = 90–100 km. As shown in Figure 1b, β_E varies between 0.14 and 0.17 km^{-1} for daytime. As for nighttime (Figure 1c), the possible range of β_E is from 0.13 to 0.15 km^{-1}.

Due to the form of the exponential term in equation (1), the range of β_E from 0.13–0.17 km^{-1} corresponds to an exponential factor ranging from −0.02 to 0.02. For β_E values less than 0.15 km^{-1}, the electron density above h_k decreases exponentially with the altitude. This feature, to some extent, resembles the E-region valley utilized in the five-parameter ionospheric model of *Cummer and Inan* [2000]. Note that the sporadic E region is not fully captured by our four-parameter model and could be important for VLF measurements in the E-region. This effect is left for investigation in our next-step study.

3 Full Wave Model

With this modified WS profile, we have calculated the expected signals from the NWC (19.8 kHz, 21.82°S, 114.17°E), NPM (21.4 kHz, 21.42°N, 158.15°W), and NAA (24 kHz, 44.65°N, 67.28°W) transmitters under all h', β_D, β_E, and h_k combinations, namely all possible ionospheric conditions. For this calculation, we utilize a well-calibrated full-wave model (FWM); details of this model can be found in *Lehtinen and Inan* [2008, 2009]. In short, this model is a computationally-efficient approach for finding the full wave solution to Maxwell's equations in a horizontally-stratified medium, given a background magnetic field and altitude profiles of electron density and collision frequency. This model works by dividing the simulation domain into a series of horizontal slabs; FWM calculates the electromagnetic field within each slab and the reflection coefficient at each slab boundary. The reflection coefficients are computed using a method inspired by *Wait* [1970] in order to avoid the numerical "swamping" instability, which has been a long-lasting concern in earlier full wave method efforts [*Nygrén*, 1982].

Considering the large number of possible parameter combinations (h', β_D, β_E, and h_k) and the resultant prohibitive computational cost, we opt to utilize the two-dimensional (2D, range and altitude) version of this FWM. Specifically, for the present study, we simulate transmitter signals up to 1500 km away from the transmitter in the radial direction, and up to the upper boundary of the E-region in the vertical direction. The altitude range between the ground and 150 km is divided into slabs with 1 km thickness. The background collision frequency profile is obtained from *Vuthaluru et al.* [2002], as previously used in *Lehtinen and Inan* [2009]; *Cohen et al.* [2012]. The geomagnetic field is assumed to be invariant with altitude and a typical value of the geomagnetic field near each transmitter is used, as taken from the IGRF model [*Macmillan and Maus*, 2005]. To mimic all ionospheric conditions, we vary h' between 65 and 90 km with 1 km steps, β_E between 0.3 and 0.8 km^{-1} with 0.01 km^{-1} steps, h_k between 90 and 100 km with 5 km steps, and β_E between 0.13 and 0.17 km^{-1} with 0.01 km^{-1} steps, amounting to a total of 19,890 simulations for each transmitter.

This FWM model has been extensively used to predict the behavior of the electromagnetic field due to a variety of natural and artificial sources [*Cohen and Inan*, 2012; *Cohen et al.*, 2012; *Lehtinen et al.*, 2010; *Graf et al.*, 2013] and, in general, good agreement with observational data and/or other numerical models has been obtained. This model has been experimentally validated using spacecraft measurements of transmitter power at 600–700 km [*Cohen and Inan*, 2012; *Cohen et al.*, 2012]. Using DEMETER data, *Cohen and Inan* [2012] first calculated the total power injected into the magnetosphere from 10 VLF transmitters, and these data were later compared with estimates calculated using present FWM model

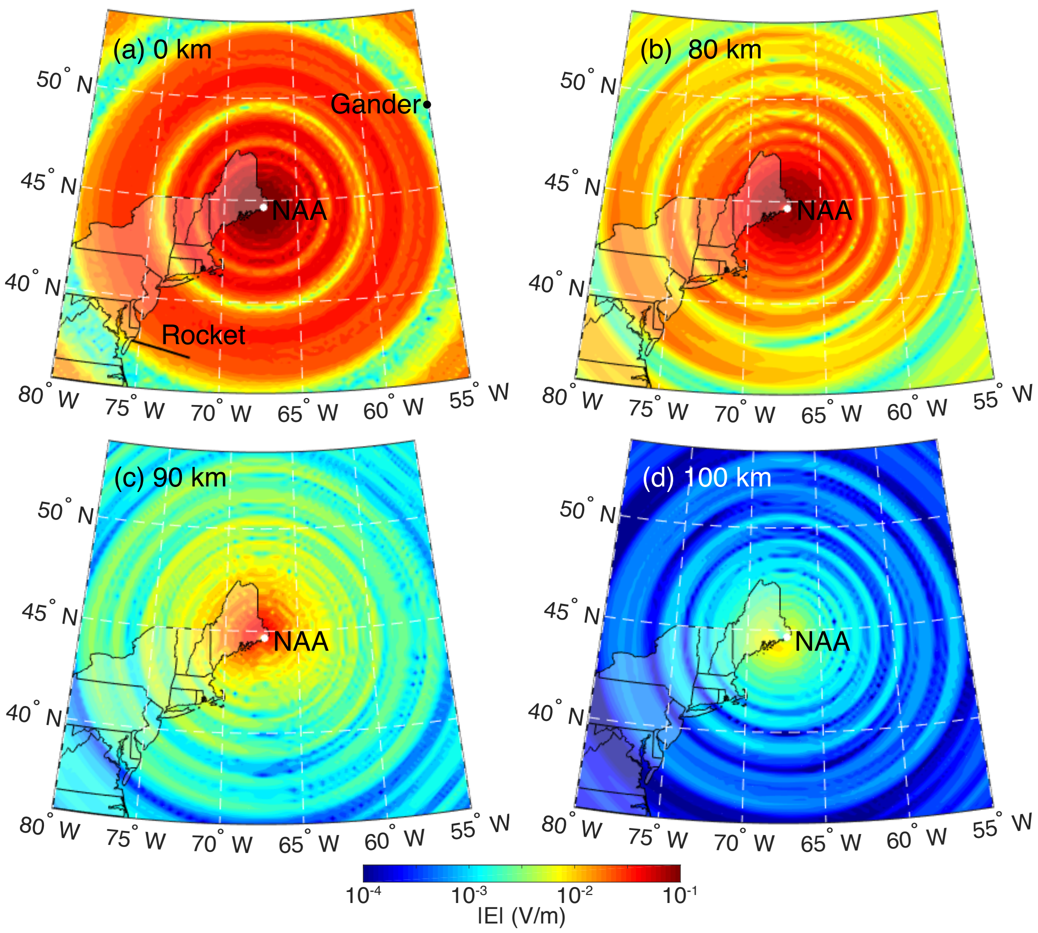

218 **Figure 2.** Full wave modeling results of the electric field amplitude at (a) ground level, (b) 80 km, (c) 90 km, and (d) 100 km altitude at different latitudes and longitudes near the NAA transmitter. The background electron density profile used in this simulation is obtained from the FIRI model, corresponding to the 50th percentile of nighttime conditions. The white dot marks the location of NAA transmitter; the black dot in the upper left panel marks Gander, Newfoundland; the black line in panel (a) shows the trajectory of a rocket that is currently under development for studying VLF propagation/attenuation in the ionosphere.

[*Cohen et al.*, 2012]. Results showed very good agreement with DEMETER data, to within several dB for both daytime and nighttime and for all transmitters considered. In the studies of lightning discharge, this model has also been employed to calculate the ground wave produced by the return stroke current [*Zoghzoghy*, 2015], and the results are well in line with both analytical solutions and a well-validated Finite Difference Time Domain (FDTD) model [*Marshall*, 2012].

Before being used for transmitter simulations, we validate this FWM model again by comparing our results with previously reported measurements of transmitter signals [*Rodriguez et al.*, 1994]. *Rodriguez et al.* [1994] studied the heating of the nighttime D-region ionosphere by VLF transmitters and reported the NAA signal recorded by their receiver located in Gander, Newfoundland; the measured electric field was approximately 13 mV/m at 01:19:30 UT on December 6, 1992. Figure 2 shows our full-wave modeling results of the electric field at ground level, 80, 90, and 100 km altitudes at different latitudes and longitudes near the NAA transmitter. The background electron density profile used in this simulation is obtained from the FIRI model, corresponding to the 50th percentile of nighttime conditions. The white dot marks NAA, while the black dot in the upper left panel marks Gander, Newfoundland.

Our model predicts an electric field amplitude of 5 mV/m in Gander, not unreasonably different from the 13 mV/m reported in *Rodriguez et al.* [1994]. We emphasize that, if a different ionosphere electron density and/or collision frequency profile were to be used, the interference pattern on the ground, for example, the ring structure in Figure 2a, could be shifted inward, towards NAA and our results in that case become even closer to Gander measurements [*Rodriguez et al.*, 1994]. For the sake of comparison, these results are calculated using the three-dimensional (3D) version of the FWM model. However, 3D simulation is extremely computationally expensive and the 2D version is used for the simulation of transmitter signal under all h', β_{D}, β_{E}, and h_{k} combinations, as will be shown in Section 4.

4 Lookup Table of Transmitter Signal

In section 4.1, we present full-wave modeling results of the expected signal along a rocket trajectory and along the ground from the NAA transmitter. The rocket trajectory is based on that planned for the VIPER sounding rocket campaign developed at UC Berkeley (Bonnell, private communication, 2020). It is representative of a trajectory well away from a VLF source (NAA, in this case) that samples the EI waveguide, the absorption and reflection layers in the D- and E-region ionosphere, and the leakage out along the B-field above. These results are plotted to showcase how the VLF propagation varies in the vertical (rocket trajectory) and horizontal (ground level) directions with respect to different h', β_{D}, β_{E}, and h_{k} values. We explain, in section 4.2, how the lookup table of transmitter signal amplitude under different h', β_{D}, β_{E}, and h_{k} combinations can be utilized to estimate the altitude profile of the ionosphere electron density. Moreover, by assuming a pair of ground receivers at different distances from the transmitter, we evaluate the sensitivity of different receiver locations at remote sensing the lower-ionosphere density, in Section 4.3. For consistency, in this section, we use the electric field results to show the dependence of VLF propagation on the above-mentioned four parameters and, since a major goal of this work is the transionospheric attenuation of VLF waves, we mainly focus on the amplitude results. Note that phase data also provide useful information for subionospheric VLF remote sensing [e.g., *Marshall et al.*, 2017; *Xu et al.*, 2019], but are not the main focus of present study.

4.1 Transmitter Signal along Rocket Trajectory and at Ground Level

Figure 3 shows full wave modeling results of the transmitter signal along a rocket trajectory. This set of simulation results shows how VLF propagation in the vertical direction varies under different ionospheric conditions. This rocket is currently under development, but planned to be launched from Wallops Island, VA during nighttime conditions. Its tra-

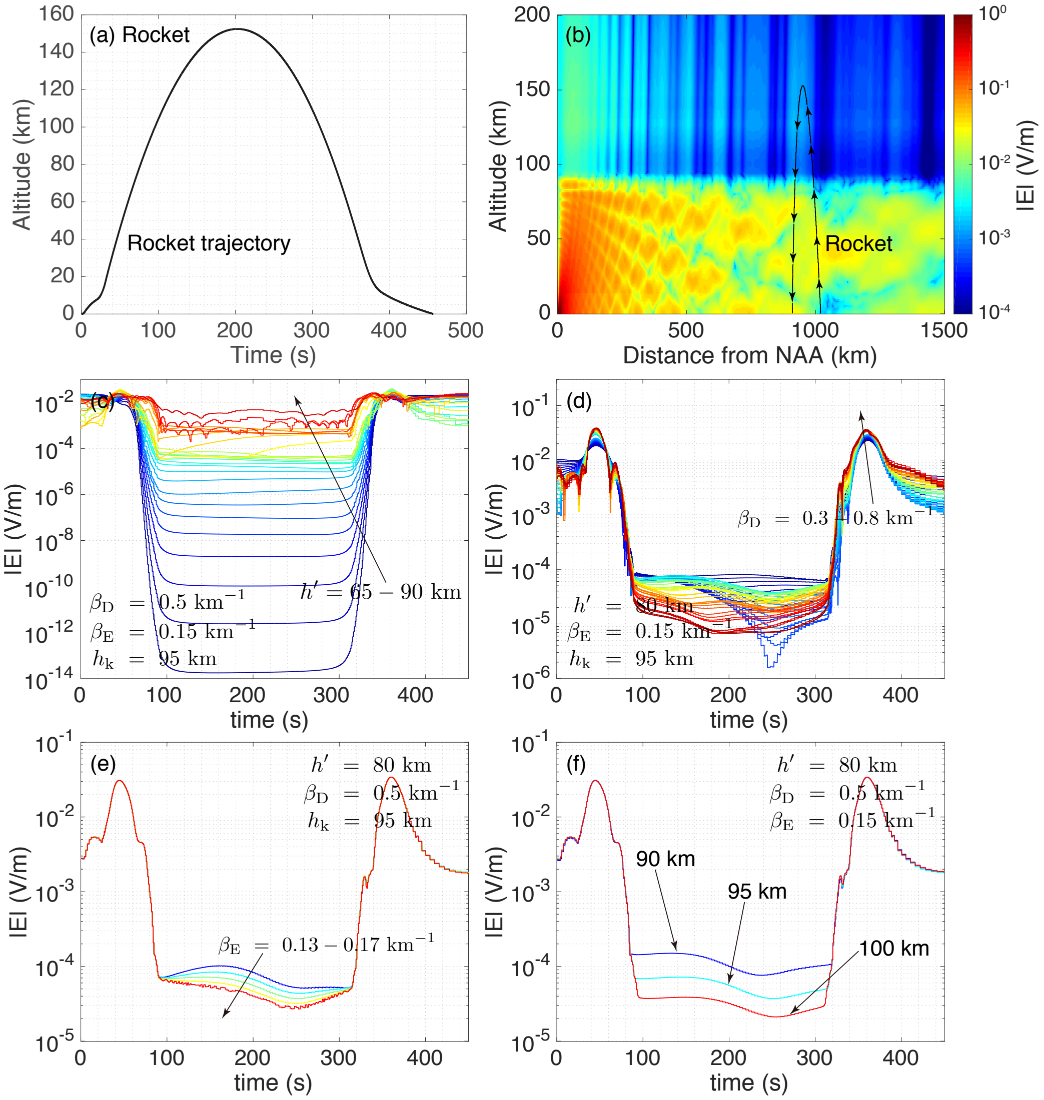

Figure 3. (a) Rocket trajectory: altitude versus time after launch. (b) Full wave modeling results of the electric field at different radial distances and altitudes from the NAA transmitter. The background electron density profile is obtained from FIRI, corresponding to the 50th percentile of nighttime conditions; the arrowed line shows the rocket trajectory as the distance from NAA versus altitude. Full wave modeling results of transmitter signal along the rocket trajectory under different (c) h', (d) β_D, (e) β_E, and (f) h_k values. In each panel, three of these four parameters are held constant and we vary the other parameter to check the key dependences. The baseline value of h', β_D, β_E, and h_k is 80 km, 0.5 km^{-1}, 0.15 km^{-1}, and 95 km, representing typical nighttime conditions. In these calculations, we vary h' between 65 and 90 km with 1 km steps, β_E between 0.3 and 0.8 km^{-1} with 0.01 km^{-1} steps, h_k between 90 and 100 km with 5 km steps, and β_E between 0.13 and 0.17 km^{-1} with 0.01 km^{-1} steps.

jectory is shown in Figure 2a and Figures 3a–3b. Figure 2a shows the latitude and longitude pair of the rocket trajectory, Figure 3a shows the rocket altitude versus time after launch, and the arrowed line in Figure 3b shows the rocket altitude versus the radial distance from NAA. The background color plot in Figure 3b shows 2D-FWM simulation results of the electric field near the NAA transmitter; the background electron density profile used in this simulation is the same as that in Figure 2, the 50th percentile of nighttime FIRI profiles.

Figure 3c shows the expected signal from the NAA transmitter along the rocket trajectory for different h' values. In this figure, β_{D} is fixed to be 0.5 km^{-1}, β_{E} is 0.15 km^{-1}, h_{k} is 95 km, and we vary h' between 65 and 90 km. Similar to a controlled experiment, these results are plotted to illustrate the dependence of expected rocket measurements of the electric field magnitude on the reflection altitude of VLF waves. Comparing this figure to Figure 3a, the simulated field results at the first ~80 s and after ~320 s are transmitter signals within the EI waveguide, while the results in between show the fraction of the NAA emission that leaks into the higher ionosphere. As h' increases from 65 to 90 km (from dark blue to red), the transmitter signal within the E-region ionosphere (between 80 and 320 s) increases by almost ten orders of magnitude. A change of h' from 65 to 90 km resembles a typical day-night transition and a higher h' value corresponds to lower electron density in the D-region, resulting in less electron-neutral collisions and less attenuation of VLF energy.

Figures 3d–3f similarly show the dependence of the transmitter signal along the rocket trajectory on β_{D}, β_{E}, and h_{k}. In these plots, three of the four parameters are held constant and we vary the remaining parameter to quantify the dependence. The baseline value of h', β_{D}, β_{E}, and h_{k} is 80 km, 0.5 km^{-1}, 0.15 km^{-1}, and 95 km, representing typical nighttime ionosphere conditions. β_{D} describes the steepness of the electron density profile below h_{k}, and changing this parameter affects the interference pattern of VLF waves within the EI waveguide, but its influence on the transmitter signal along the rocket trajectory is highly nonlinear, as shown in Figure 3d.

With the definition in equation (1), h' and β_{D} control the propagation of VLF waves in both D- and E-region ionosphere, whereas β_{E} and h_{k} are solely related to the E-region, corresponding to the rocket results between ~80 and ~320 s in Figure 3. The electron density in the E-region ionosphere decreases exponentially with altitude if β_{E} is smaller than 0.15 km^{-1}, and increases if β_{E} is greater than 0.15 km^{-1}. As β_{E} increases from 0.13 to 0.17 km^{-1}, a weaker transmitter signal is expected along the rocket trajectory since the electron density in the E-region ionosphere, in essence, becomes higher with larger β_{E} values, and VLF waves are more severely attenuated (see Figure 3e). h_{k} has a similar effect on the rocket signal: for the same background collision frequency profile, smaller h_{k} value corresponds to lower electron density in the E-region ionosphere and less VLF absorption.

Figure 4 shows the transmitter signal at ground level versus the radial distance from NAA. Different from the rocket results, this plot shows a slice of the EI waveguide in the horizontal direction. Similar to Figure 3, either h' or β_{D} is held constant in this figure and we vary the other parameter to quantify the dependence. Note that VLF propagation within the EI waveguide is governed by h' and β_{D}, and these are the only free parameters in Figure 4. The baseline value is 75 km for h', and 0.4 km^{-1} for β_{D}. We vary h' between 65–90 km and β_{D} between 0.3–0.8 km^{-1}.

The simulated ground signals in Figure 4 exhibit nulls and enhancements at ranges between ~300 and ~1300 km. An amplitude "null" refers to the local minima in the VLF signal; for example, the major null indicated by the green ring in Figure 2a and the valley of the red curve (h' value of 90 km) around ~1250 km in Figure 4a. It is specifically caused by the interference among propagating waveguide modes, for example, two modes with similar amplitudes and a phase difference of 180° would cancel each other and give rise to a local minimum in VLF measurements. Figure 4a shows the dependence of the transmitter signal at ground level on the reflection altitude. One sees clearly that, as h' increases, VLF waves are reflected at higher altitudes and the amplitude null shifts further away from the VLF

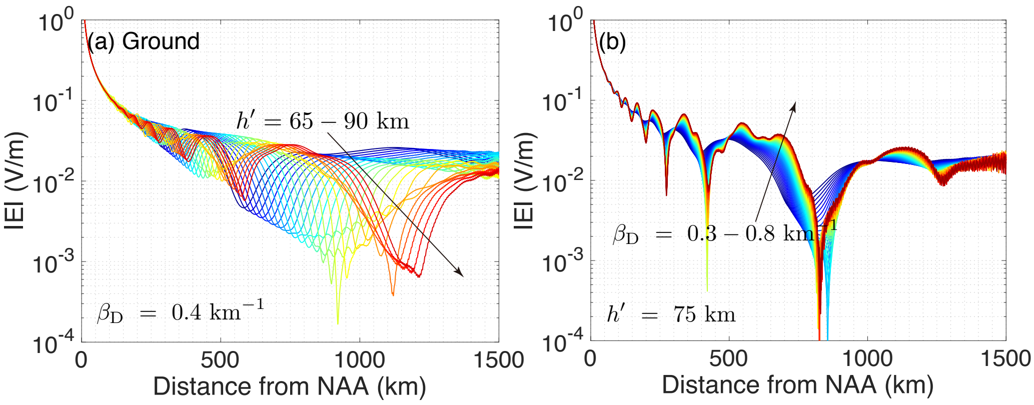

Figure 4. (a) Full wave modeling results of the expected signal from the NAA transmitter at ground level. In this plot, β_{D} is fixed to be 0.4 km^{-1} and we vary h' between 65 and 90 km with 1 km interval. Panel (b) shows similar results, but for the h' value of 75 km and β_{D} values between 0.3 to 0.8 km^{-1}.

transmitter. The effects of β_{D} on modal interference pattern are less prominent than h'. As shown in Figure 4b, for β_{D} values between 0.3 and 0.8 km^{-1}, the location of the nulls does not change noticeably and the main change is the field amplitude.

4.2 Remote Sensing Lower-Ionosphere Electron Density

The results presented in the previous section show part of the lookup table that we calculate for the NAA transmitter and for all h', β_{D}, β_{E}, and h_{k} combinations. This lookup table can be readily used, in conjunction with VLF measurements, for D- and E-region inversion and remote sensing. To illustrate this idea, we have conducted a numerical experiment using FIRI profiles. Specifically, a separate set of FWM simulations is performed using the 1,980 FIRI profiles as the background ionospheres. Four simulated ground receivers are assumed to be placed at distances of 16, 413, 914, and 1012 km away from NAA (these receiver locations are planned to provide the ground observation in support of the VIPER rocket mission).

We first calculate the transmitter signal at these four receiver locations using the FWM simulation with different FIRI profiles; these results are regarded as "synthetic" ground measurements (denoted as simulated measurements hereafter) and the associated FIRI profile represents the true ionosphere condition – truth data against which we can examine if the electron density profile derived from the lookup table is reasonable. For these calculations, the FIRI profiles at altitudes above 55 km are used. The black curve in Figure 5a shows an example of the simulated measurements and the four dots mark the receiver locations. The simulated measurements at the four receivers are then compared with the lookup-table results with different h' and β_{D} values (colored lines in Figure 5a). We calculate the sum of squared residuals between base-10 logarithms of the simulated measurements and different h' and β_{D} results, as shown in Figure 5b. Finally, the pair of h' and β_{D} that minimizes the sum of squared residuals is determined as the best fit.

Figure 5c shows the best-fit found from all h' and β_{D} combinations to the simulated measurements in Figure 5a. The best-fit h' value is 81 km and β_{D} value is 0.45 km^{-1}. Knowing h' and β_{D}, we can reconstruct the altitude profile of electron density using equation (1), and this represents our guess of the ionosphere condition, which is shown as the blue curve in Figure 5d, while the black curve is the FIRI profile used for simulated measurements. Since h' and β_{D} describe the electron density up to the knee altitude, in Figure 5d, we only compare the electron density below 90 km. It is clear that the electron density profile derived

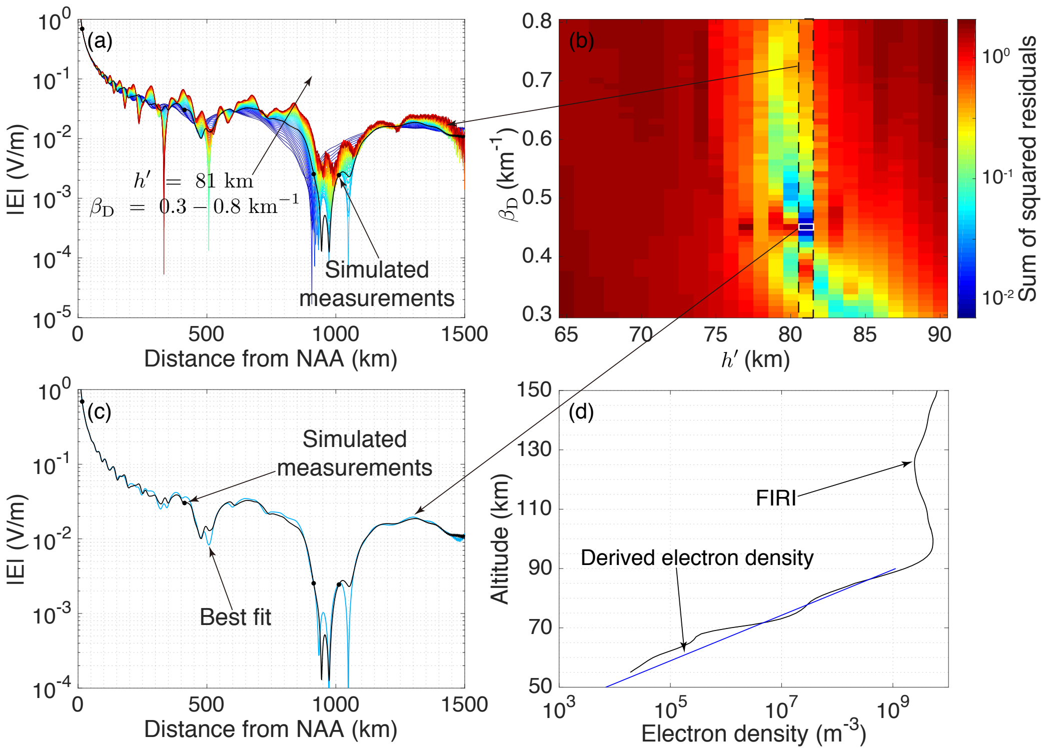

377 **Figure 5.** (a) Simulated ground measurements from the NAA transmitter. The black dots mark the receiver
378 locations that we use to find out the best-fit h' and β_D. The background electron density profile is obtained
379 from FIRI and shown as the black curve in panel (d). The colored lines show lookup table results with an h'
380 value of 81 km and β_D values of 0.3–0.8 km^{-1}. (b) Sum of squared residuals between base-10 logarithms of
381 simulated measurements at the four receivers and lookup table results corresponding to different h' and β_D
382 combinations. (c) The best-fit to the simulated measurements at the four receivers. The best-fit h' value is
383 81 km and β_D value is 0.45 km^{-1}. (d) Comparison between the true FIRI profile used for simulated measure-
384 ments and the electron density profile derived from the best-fitting h' and β_D values.

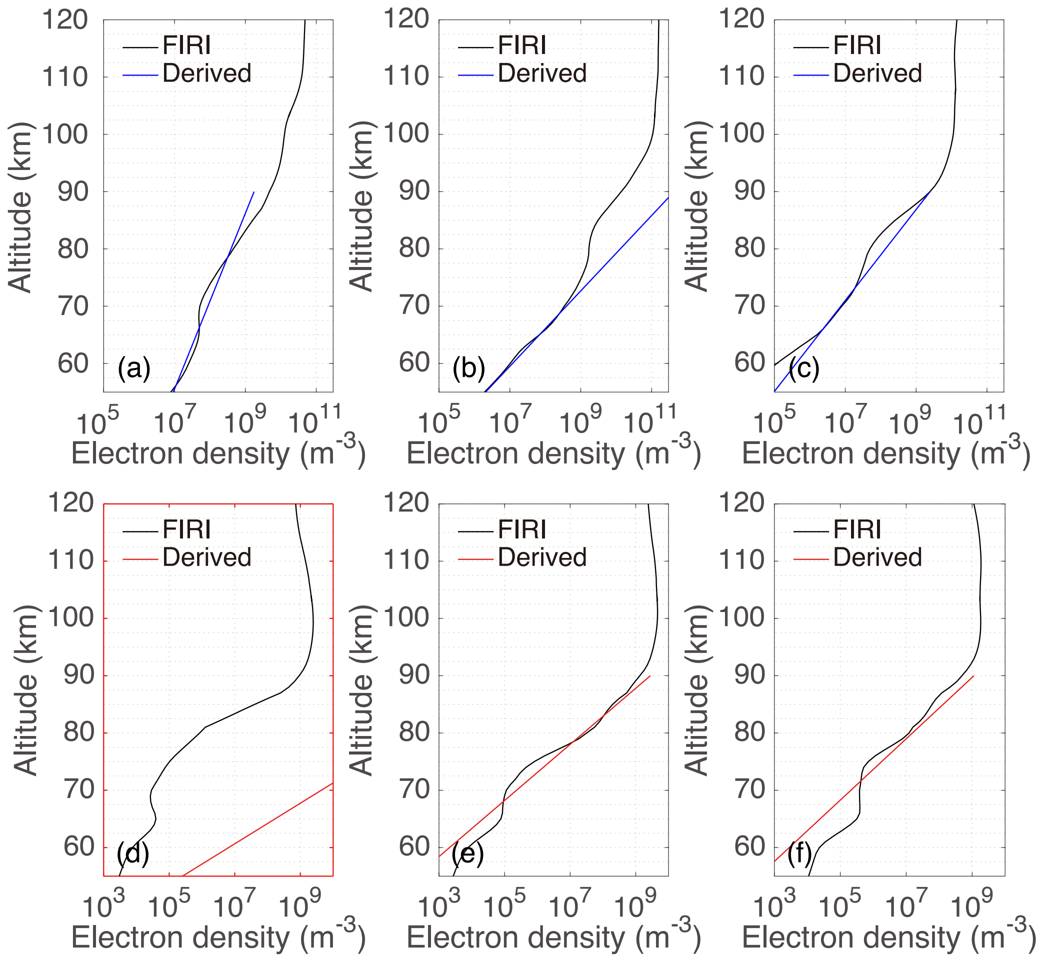

Figure 6. Comparison between the true FIRI profiles and those derived from the comparison with lookup table for typical (upper panels) daytime and (bottom panels) nighttime conditions.

from our lookup table is fairly consistent with the true FIRI profile at altitudes below 90 km. Note that ground measurements are solely controlled by h' and β_D in our four-parameter model. Therefore, we have only searched in the parametric space of these two parameters for the best-fit. If rocket or space-borne measurements are instead used, a complete search in all the parameters will be performed.

We have repeated this calculation for all FIRI profiles, including a total of 1,620 profiles for daytime ionospheres and 360 for nighttime ionospheres. Figure 6 shows the comparison between 6 FIRI profiles and those deduced from the lookup table; the upper panels show the comparison for daytime profiles, while the bottom panels show those of nighttime. These 6 comparisons are randomly chosen out of the 1,980 FIRI profiles to show the goodness of fit. Except for the comparison in Figure 6d, the derived electron density profiles in general agree very well with the true FIRI profiles in terms of both magnitude and sharpness, in particular at altitudes near and just below the nominal VLF reflection height.

To quantitatively evaluate the lookup-table results, we have calculated the percentage difference in electron density between the derived and true FIRI profiles; the average value at altitudes between 65 and 80 km is calculated as a measure of goodness-of-fit. This altitude range is used from two considerations: 1) VLF signals are sensitive to the electron density

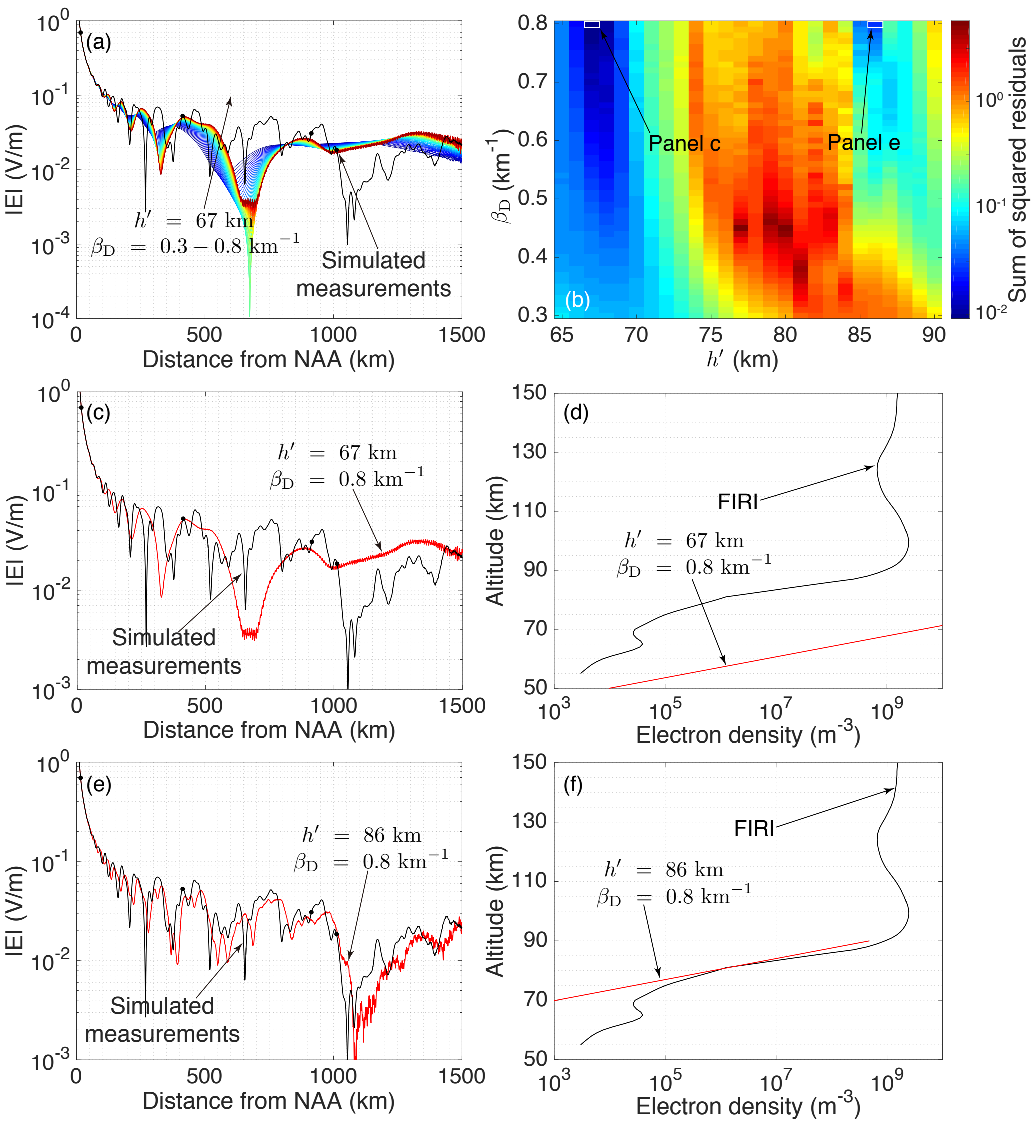

Figure 7. The first four panels are similar to Figure 5, but for the FIRI profile (black curve) shown in Figure 6d. (e) Comparison between the simulated measurements and lookup table results corresponding to h' = 86 km and β_D = 0.8 km^{-1}. (f) Comparison between this pair of h' and β_D and the true FIRI profile.

variation in this altitude range and it is critical for VLF reflection; and 2) the FIRI profiles are suggested [*Friedrich et al.*, 2018] to be valid at altitudes above 60 km and electron density larger than 10^6 m^{-3} (see Figure 1). In 1,131 out of 1,980 cases, the average difference between the derived and true FIRI profiles is found to be less than 80%. A difference of 80% at altitudes between 65 and 80 km is not as significant as it appears to be, considering how sharply the electron density profile is changing in this altitude range; the electron density increases by nearly three orders of magnitude from 65 to 80 km, but a simple exponential function is utilized to describe this change. If we define good estimation as a mean error of less than 100% from the true FIRI profile, the good-estimation rate is 77% for daytime profiles, and 74% for nighttime profiles.

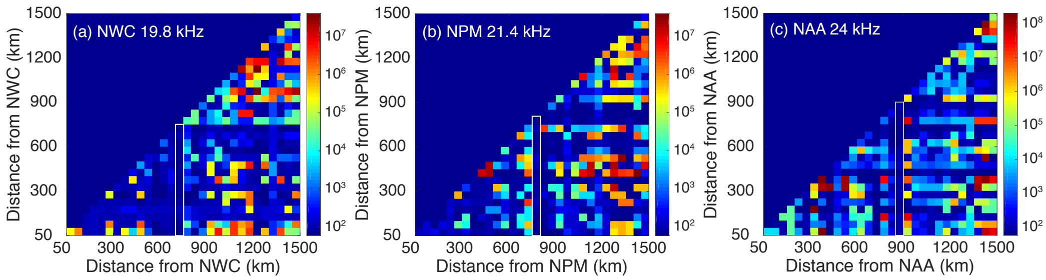

Figure 8. Sensitivity of different receiver locations in remote sensing the lower-ionosphere electron density. (a) Average value of the mean difference in electron density (at altitudes of 55–90 km) between 1,980 FIRI profiles and those derived from the lookup table. The electron density profile is derived from the comparison with the NWC lookup table using simulated measurements by two receivers at different distances from the NWC transmitter, as indicated by the x and y axis. Panels (b) and (c) show similar results, but for the NPM and NAA transmitter at 21.4 kHz and 24 kHz, respectively.

Figure 6d shows an example in which the lookup-table results are fundamentally different from the truth and we explain this example with more details in Figure 7. Note that the discrepancy in Figure 6d is not caused by the altitude and electron-density limitation of FIRI profiles, but by the constraint used in our lookup-table calculation. Figures 7a–7d show similar results as Figure 5, but for the FIRI profile shown in Figure 6d. The minimum value in the sum of squared residuals is obtained with an h' value of 67 km and β_{D} value of 0.8 km^{-1} (Figure 7b). As shown in Figure 7c, the simulated measurements at the four receiver locations can be satisfactorily fitted using this pair of h' and β_{D}, but the overall ground pattern, as well as the location of amplitude nulls, are distinctly different from the truth.

A best-fit value of 68 km for h' is indicative of daytime ionosphere conditions, while the best-fit β_{D} value is typical of nighttime conditions. The ionosphere electron density described by h' = 68 km and β_{D} = 0.8 km^{-1} is too steep and likely unrealistic for normal daytime conditions, unless with substantial ionosphere enhancements due to, for example, solar flare events. If instead we constrain the parametric search to nighttime h' values, the next best-fit is h' = 86 km and β_{D} = 0.8 km^{-1}. The comparison between this pair of h' and β, and the simulated measurements and true FIRI profile is shown in Figures 7e and 7f, respectively. The interference pattern along the ground in this case becomes noticeably closer to the simulated measurements (Figure 7e). It is thus not surprising that the corresponding electron density profile becomes consistent with the truth.

4.3 Ground Receiver Placement

The example in Figure 7, to some extent, highlights the importance of receiver placement in determining the ionosphere density profiles. The four receivers that we use are not optimally located to reconstruct the interference pattern produced by the FIRI profile shown in Figure 7f. The electron density profile calculated from our lookup-table inversion is thus non-unique; multiple h' and β_{D} combinations can provide almost equal goodness in fitting the simulated measurements at the four receivers (see Figures 7c and 7e). If the fourth receiver (1012 km) is instead placed slightly further away from the transmitter at ~1050 km, the major amplitude null would be then captured (the black curve at ~1050 km in Figure 7e). In this scenario, the pair of h' and β_{D} that we originally determined as the best-fit is no longer consistent with the VLF signal at this location (see Figure 7c), while the pair of h' and β_{D} in Figure 7e becomes consistent. A receiver location at ~1050 km is therefore more effective in inferring the ionosphere parameters than the 1020 km location, for this particular FIRI ionosphere (Figure 7f). From this consideration, we attempt to evaluate the sensitivity of different receiver locations in probing the ionosphere electron density.

To this end, two ground receivers are considered; these two receivers can be placed at any location between 50 and 1500 km away from the transmitter with a step size of 50 km. For each pair of receiver locations, we repeat the calculation described in section 4.2: we simulate VLF measurements at the two receiver locations using 1,980 FIRI profiles; for each FIRI profile, the simulated measurements by the two receivers are compared with the lookup table in order to find out the best-fit h' and β_{D}; after obtaining the best-fit h' and β_{D}, we calculate the mean percentage difference in electron density at altitudes of 55–90 km between the derived and FIRI profiles. The average value of this difference in electron density over 1,980 FIRI profiles is then computed and considered as a measure of the sensitivity for this pair of receiver locations. These results for different combinations of receiver locations are shown in Figure 8 for the NWC, NPM, and NAA transmitters with different frequencies.

Locations near the major amplitude null are more suitable for the purpose of lower-ionosphere remote sensing. The pair of receiver locations that yields the smallest difference between the derived and FIRI profiles is 250 and 800 km away from NWC. The best locations are 550 and 950 km for NPM, and 950 and 1050 km for NAA. Moreover, it is interesting to observe that this average difference is in general smaller if one of the two receivers is placed at a distance of 750 km away from NWC, 800 km away from NPM, and 900 km away from NAA (marked as white boxes in Figure 8). Nearly all these receiver locations, as suggested by our simulation results, are close to the major amplitude null corresponding to nighttime h' values (see Figure 4a). The main reason for the improved performance at these locations is that the VLF signal near the amplitude null exhibits greater variation compared to other locations and is more sensitive to the change in ionosphere parameters (see Figure 4). Nevertheless, we emphasize that the goal of this calculation is not to find out the optimal location for all ionospheric conditions, but to evaluate the sensitivity of different receiver locations. For a given ionospheric condition, multiple receiver locations can work almost equally well in estimating the ionospheric parameters, but their performance may become worse if the ionospheric condition changes. In general, Figure 8 shows that there are numerous pairs of receiver locations that would provide good estimation, and other locations that would perform poorly. This figure thus provides a tool that researchers can use to plan ground VLF transmitter experiments, based on the specific needs and ionospheric conditions.

5 CONCLUSION AND DISCUSSION

For the purpose of transionospheric VLF modeling, as well as D- and E-region remote sensing, we have parameterized the FIRI profiles in this study on the basis of the widely-used WS profile and we extend the WS profile to higher altitudes by introducing two parameters for the E-region ionosphere. Using the modified WS profile and a well-validated FWM model, we have further tabulated the expected transmitter signal at different locations from NWC, NPM, and NAA under all possible ionospheric conditions. We note that the WS profile has been previously extended by *Cummer and Inan* [2000] to E-region altitudes for ionospheric remote sensing using lightning-emitted ELF waves. However, the parameters utilized in the present study for the E-region ionosphere are different from those of *Cummer and Inan* [2000], as well as the method of electron density remote sensing.

The transmitter signal lookup table reported herein can be readily used for the inversion and remote sensing of the D- and E-region ionosphere. We have tested this lookup table using FWM simulation and 1,980 FIRI profiles. In 1,131 out of 1,980 cases, the average difference between the derived and true FIRI profile at altitudes between 65 and 80 km is less than 80%. Our lookup table achieves a good-estimation (average difference $\leq$ 100%) rate of 77% for daytime FIRI profiles, and 74% for nighttime FIRI profiles.

By approximating the electron density in the D- and E-region ionosphere using four parameters, this opens the possibility for pre-tabulating the VLF responses to all ionospheric conditions, namely a lookup table. The lookup table reported herein are broadly applicable to ionospheric remote sensing using ground and/or rocket measurements, the planning of VLF receivers (Figure 8), as well as transionsopheric VLF attenuation, even though they have only been tested using FWM-simulated ground measurements in this study. For improving this validation, we plan on comparing our inversion results with in situ measurements of both the VLF wave field and background neutral and plasma properties, i.e., measurements from the VIPER rocket mission mentioned in section 4.1. To better understand transionospheric VLF propagation and develop a remote sensing method for the rocket measurements represents the overarching goal of our study. As the first step, we develop and validate a method that will be utilized in the analysis of rocket data, as reported in this paper. The comparison of in situ versus remotely-sensed ionospheric profiles represents the goal of our second-step study.

A constrained search can largely improve the correctness of the lookup-table calculation, as evidenced in Figure 7. Depending on the solar zenith angle or perturbation from the radiation belts or sun, certain combinations of h', β_{D}, β_{E} and h_{k} become unrealistic and these need to be excluded while searching for the best-fit. Of note, the present lookup table is obtained under the assumption that the background electron density in the horizontal direction is invariant and homogeneous. *Cummer et al.* [1998] have tested this assumption using simulation of lightning sferics, and found that VLF propagation is dominantly controlled by the path-averaged ionosphere characteristics. As such, the best-fitting parameters derived from the comparison with our lookup table represent the average ionosphere condition for the path between the transmitter and receiver. Furthermore, present results suggest that receiver locations near the major amplitude null are more sensitive to the variation in ionosphere parameters, therefore more suitable for the purpose of remote sensing.

Terrestrial VLF energy from both lightning discharge and ground-based VLF transmitters is important for the dynamics of the slot region and the inner radiation belt [e.g., *Abel and Thorne*, 1998a,b; *Bortnik et al.*, 2006a,b; *Hua et al.*, 2020]. To study these effects from a modeling perspective, we need more accurate understanding of the total input of terrestrial VLF energy into the radiation belts. Previous studies on this topic were mostly based on the absorption curve of VLF waves calculated using a handful of ionosphere profiles, which only provided the statistical bounds on VLF absorption. For more thorough studies, it is essential to generalize the FIRI profiles and develop a parameterized model for the altitude range in which VLF waves are attenuated. The modified WS profile reported herein fulfills this need: it is eminently suitable for full characterization of VLF propagation under different ionosphere conditions, ultimately facilitating quantification of the effects on the radiation belts brought by terrestrial VLF energy.

Acknowledgments

This research was supported by the NASA grant 80NSSC18K0782 and NSF grant AGS-1952465. J. Bortnik's research was supported by VIPER subgrant 00009841 from UC Berkeley under NASA Prime Grant agreement, 80NSSC18K0782. J. W. Bonnell's research was supported by the NASA LCAS Program Grant 80NSSC18K0782. The simulation data and analysis codes used to generate all figures and results in this paper are available at https://doi.org/10.5281/zenodo.4556032.

References

Abel, B., and R. M. Thorne (1998a), Electron scattering loss in Earth's inner magnetosphere: 1. Dominant physical processes, *J. Geophys. Res. Space Physics*, *103*(A2), 2385–2396.

Abel, B., and R. M. Thorne (1998b), Electron scattering loss in Earth's inner magnetosphere: 2. Sensitivity to model parameters, *J. Geophys. Res. Space Physics*, *103*(A2), 2397–2407.

Bilitza, D. (2001), International reference ionosphere 2000, *Radio Science*, *36*(2), 261–275.

Bilitza, D., and B. W. Reinisch (2008), International reference ionosphere 2007: Improvements and new parameters, *Adv. Space Res.*, *42*(4), 599–609.

Bortnik, J., U. S. Inan, and T. F. Bell (2006a), Temporal signatures of radiation belt electron precipitation induced by lightning-generated MR whistler waves: 1. Methodology, *J. Geophys. Res. Space Physics*, *111*, A02204.

Bortnik, J., U. S. Inan, and T. F. Bell (2006b), Temporal signatures of radiation belt electron precipitation induced by lightning-generated MR whistler waves: 2. Global signatures, *J. Geophys. Res. Space Physics*, *111*, A02205.

Brasseur, G. P., and S. Solomon (2006), *Aeronomy of the middle atmosphere: chemistry and physics of the stratosphere and mesosphere*, 3rd ed., Springer, Dordrecht, The Netherlands.

Budden, K. G. (1998), *Radio Waves in the Ionosphere*, Cambridge University Press, United Kingdom.

Claudepierre, S. G., Q. Ma, J. Bortnik, T. P. O'Brien, J. F. Fennell, and J. B. Blake (2020a), Empirically estimated electron lifetimes in the Earth's radiation belts: Comparison with theory, *Geophys. Res. Lett.*, *47*(3), e2019GL086,056, doi: https://doi.org/10.1029/2019GL086056.

Claudepierre, S. G., Q. Ma, J. Bortnik, T. P. O'Brien, J. F. Fennell, and J. B. Blake (2020b), Empirically Estimated Electron Lifetimes in the Earth's Radiation Belts: Van Allen Probe Observations, *Geophys. Res. Lett.*, *47*(3), e2019GL086,053, doi: https://doi.org/10.1029/2019GL086053.

Clilverd, M. A., C. J. Rodger, R. Gamble, N. P. Meredith, M. Parrot, J.-J. Berthelier, and N. R. Thomson (2008), Ground-based transmitter signals observed from space: Ducted or nonducted?, *J. Geophys. Res. Space Physics*, *113*, A04211.

Codrescu, M. V., T. J. Fuller-Rowell, R. G. Roble, and D. S. Evans (1997), Medium energy particle precipitation influences on the mesosphere and lower thermosphere, *J. Geophys. Res.*, *102*(A9), 19,977–19,987, doi:10.1029/97JA01728.

Cohen, M. B., and U. S. Inan (2012), Terrestrial VLF transmitter injection into the magnetosphere, *J. Geophys. Res. Space Physics*, *117*, A08310.

Cohen, M. B., N. G. Lehtinen, and U. S. Inan (2012), Models of ionospheric VLF absorption of powerful ground based transmitters, *Geophys. Res. Lett.*, *39*, L24101.

Cummer, S. A., and U. S. Inan (2000), Ionospheric E region remote sensing with ELF radio atmospherics, *Radio Science*, *35*(6), 1437–1444.

Cummer, S. A., U. S. Inan, and T. F. Bell (1998), Ionospheric D region remote sensing using VLF radio atmospherics, *Radio Sci.*, *33*(6), 1781–1792.

Foster, J. C., P. J. Erickson, D. N. Baker, A. N. Jaynes, E. V. Mishin, J. F. Fennel, X. Li, M. G. Henderson, and S. G. Kanekal (2016), Observations of the impenetrable barrier, the plasmapause, and the VLF bubble during the 17 March 2015 storm, *J. Geophys. Res. Space Physics*, *121*(6), 5537–5548.

Friedrich, M., and K. Torkar (2001), FIRI: A semiempirical model of the lower ionosphere, *J. Geophys. Res. Space Physics*, *106*(A10), 21,409–21,418.

Friedrich, M., R. Pilgram, and K. Torkar (2001), A novel concept for empirical D-region modelling, *Adv. Space Res.*, *27*(1), 5–12.

Friedrich, M., C. Pock, and K. Torkar (2018), FIRI-2018, an updated empirical model of the lower ionosphere, *J. Geophys. Res. Space Physics*, *123*(8), 6737–6751.

Fritts, D. C., and M. J. Alexander (2003), Gravity wave dynamics and effects in the middle atmosphere, *Reviews of geophysics*, *41*(1), 1003.

Graf, K. L., U. S. Inan, D. Piddyachiy, P. Kulkarni, M. Parrot, and J.-A. Sauvaud (2009), DEMETER observations of transmitter-induced precipitation of inner radiation belt electrons, *J. Geophys. Res. Space Physics*, *114*, A07205.

Graf, K. L., U. S. Inan, and M. Spasojevic (2011), Transmitter-induced modulation of subionospheric VLF signals: Ionospheric heating rather than electron precipitation, *J.*

Geophys. Res. Space Physics, *116*, A12313.

Graf, K. L., N. G. Lehtinen, M. Spasojevic, M. B. Cohen, R. A. Marshall, and U. S. Inan (2013), Analysis of experimentally validated trans-ionospheric attenuation estimates of VLF signals, *J. Geophys. Res. Space Physics*, *118*(5), 2708–2720.

Han, F., and S. A. Cummer (2010), Midlatitude daytime D region ionosphere variations measured from radio atmospherics, *J. Geophys. Res. Space Physics*, *115*, A10314.

Han, F., S. A. Cummer, J. Li, and G. Lu (2011), Daytime ionospheric D region sharpness derived from VLF radio atmospherics, *J. Geophys. Res. Space Physics*, *116*, A05314.

Helliwell, R. A. (1965), *Whistlers and related ionospheric phenomena*, vol. 50, Stanford University Press Stanford, Calif.

Hosseini, P., M. Gołkowski, and V. Harid (2019), Remote sensing of radiation belt energetic electrons using lightning triggered upper band chorus, *Geophys. Res. Lett.*, *46*(1), 37–47, doi:10.1029/2018GL081391.

Hua, M., W. Li, B. Ni, Q. Ma, A. Green, X. Shen, S. G. Claudepierre, J. Bortnik, X. Gu, S. Fu, et al. (2020), Very-Low-Frequency transmitters bifurcate energetic electron belt in near-earth space, *Nature communications*, *11*(1), 1–9.

Imhof, W. L., J. B. Reagan, H. D. Voss, E. E. Gaines, D. W. Datlowe, J. Mobilia, R. A. Helliwell, U. S. Inan, J. Katsufrakis, and R. G. Joiner (1983), Direct observation of radiation belt electrons precipitated by the controlled injection of VLF signals from a ground-based transmitter, *Geophys. Res. Lett.*, *10*(4), 361–364.

Inan, U. S., S. A. Cummer, and R. A. Marshall (2010), A survey of elf and vlf research on lightning-ionosphere interactions and causative discharges, *J. Geophys. Res. Space Physics*, *115*, A00E36.

Jursa, A. S. (Ed.) (1985), *Handbook of Geophysics and the Space Environment*, US Air Force Geophysics Lab., Springfield, VA.

Lehtinen, N. G., and U. S. Inan (2008), Radiation of ELF/VLF waves by harmonically varying currents into a stratified ionosphere with application to radiation by a modulated electrojet, *J. Geophys. Res. Space Physics*, *113*, A06301.

Lehtinen, N. G., and U. S. Inan (2009), Full-wave modeling of transionospheric propagation of VLF waves, *Geophys. Res. Lett.*, *36*, L03104.

Lehtinen, N. G., R. A. Marshall, and U. S. Inan (2010), Full-wave modeling of “early” VLF perturbations caused by lightning electromagnetic pulses, *J. Geophys. Res. Space Physics*, *115*(A7).

Ma, Q., D. Mourenas, W. Li, A. Artemyev, and R. M. Thorne (2017), VLF waves from ground-based transmitters observed by the Van Allen Probes: Statistical model and effects on plasmaspheric electrons, *Geophys. Res. Lett.*, *44*(13), 6483–6491.

Macmillan, S., and S. Maus (2005), International geomagnetic reference field–the tenth generation, *Earth, planets and space*, *57*(12), 1135–1140.

Marshall, R. A. (2012), An improved model of the lightning electromagnetic field interaction with the D-region ionosphere, *J. Geophys. Res. Space Physics*, *117*, A03316.

Marshall, R. A., and J. B. Snively (2014), Very low frequency subionospheric remote sensing of thunderstorm-driven acoustic waves in the lower ionosphere, *J. Geophys. Res. Atmospheres*, *119*(9), 5037–5045.

Marshall, R. A., T. Wallace, and M. Turbe (2017), Finite-Difference Modeling of Very-Low-Frequency Propagation in the Earth-Ionosphere Waveguide, *IEEE Trans. on Antennas Propagat.*, *65*, 7185–7197.

McKay-Bukowski, D., et al. (2015), Kaira: The Kilpisjärvi atmospheric imaging receiver array–System overview and first results, *IEEE Trans. Geosc. Remote Sensing*, *53*(3), 1440–1451.

Mushtak, V. C., and E. R. Williams (2002), ELF propagation parameters for uniform models of the Earth–ionosphere waveguide, *J. Atmos. Solar Terr. Phys.*, *64*(18), 1989–2001.

Nygrén, T. (1982), A method of full wave analysis with improved stability, *Planetary and Space Science*, *30*(4), 427–430.

Parrot, M., J. Sauvaud, J.-J. Berthelier, and J. Lebreton (2007), First in-situ observations of strong ionospheric perturbations generated by a powerful VLF ground-based transmitter, *Geophys. Res. Lett.*, *34*, L11111.

Platino, M., U. S. Inan, T. F. Bell, M. Parrot, and E. Kennedy (2006), DEMETER observations of ELF waves injected with the HAARP HF transmitter, *Geophys. Res. Lett.*, *33*, L16101.

Rodriguez, J. V., U. S. Inan, and T. F. Bell (1994), Heating of the nighttime D region by very low frequency transmitters, *J. Geophys. Res. Space Physics*, *99*(A12), 23,329–23,338.

Starks, M. J., R. A. Quinn, G. P. Ginet, J. M. Albert, G. S. Sales, B. W. Reinisch, and P. Song (2008), Illumination of the plasmasphere by terrestrial very low frequency transmitters: Model validation, *J. Geophys. Res. Space Physics*, *113*, A09320.

Tao, X., J. Bortnik, and M. Friedrich (2010), Variance of transionospheric VLF wave power absorption, *J. Geophys. Res. Space Physics*, *115*, A07303.

Vampola, A., and G. Kuck (1978), Induced precipitation of inner zone electrons, 1. Observations, *J. Geophys. Res. Space Physics*, *83*(A6), 2543–2551.

Voss, H. D., W. L. Imhof, M. Walt, J. Mobilia, E. E. Gaines, J. B. Reagan, U. S. Inan, R. A. Helliwell, D. L. Carpenter, J. P. Katsufrakis, et al. (1984), Lightning-induced electron precipitation, *Nature*, *312*(5996), 740–742.

Vuthaluru, R., R. A. Vincent, D. A. Holdsworth, and I. M. Reid (2002), Collision frequencies in the D-region, *J. Atmos. Solar Terr. Phys.*, *64*(18), 2043–2054.

Wait, J. R. (1970), *Electromagnetic waves in stratified media*, vol. 3, Pergamon, New York.

Wait, J. R., and K. P. Spies (1964), Characteristics of the Earth-ionosphere waveguide for VLF radio waves, *Technical note 300*, National Bureau of Standards, Boulder, CO.

Xu, W., R. A. Marshall, A. Kero, E. Turunen, D. Drob, J. Sojka, and D. Rice (2019), VLF measurements and modeling of the D-region response to the 2017 total solar eclipse, *IEEE Transactions on Geoscience and Remote Sensing*, *57*(10), 7613–7622.

Yang, H., and V. P. Pasko (2005), Three-dimensional finite difference time domain modeling of the Earth-ionosphere cavity resonances, *Geophys. Res. Lett.*, *32*, L03114.

Zoghzoghy, F. G. (2015), Statistical Analysis and Modeling of Lightning Using Radio Remote Sensing, Ph.D. thesis, Stanford University.